Electrochimica Acta 466 (2023) 143059

Contents lists available at ScienceDirect

Electrochimica Acta

journal homepage: www.journals.elsevier.com/electrochimica-acta

Geometrical and chemical effects on the electrochemistry of single-wall carbon nanotube (SWCNT) network electrodes

Elli Leppänen [a], Eero Gustafsson [a], Niklas Wester [a,b], Ilkka Varjos [b], Sami Sainio [a,c,d], Tomi Laurila [a,e,*]

[a] Department of Electrical Engineering and Automation, School of Electrical Engineering, Aalto University, PO Box 13500, 00076 Aalto, Finland
[b] Canatu Oy, Tiilenlyöjänkuja 9, 00390 01720 Vantaa, Finland
[c] Stanford Synchrotron Radiation Lightsource, SLAC National Accelerator Laboratory, Menlo Park, CA, 94025, USA
[d] Microelectronics Research Unit, Faculty of Information Technology and Electrical Engineering, University of Oulu, PO Box 4500, 90570 Oulu, Finland
[e] Department of Chemistry and Materials Science, School of Chemical Engineering, Aalto University, PO Box 16200, 00076 Aalto, Finland

ARTICLE INFO

Keywords:
Single-walled carbon nanotubes
X-ray absorption spectroscopy
Electrochemistry
Structure-property relationship

ABSTRACT

Single-wall carbon nanotube (SWCNT) network is a promising electrode material for bio detection. Unfortunately, the associations between their physical as well as chemical properties and observed electrochemical performance are not known. This hinders any systematic optimization of the network properties towards specific analytes. Here we present a consistent physicochemical and electrochemical characterization of differently treated SWCNT networks. The results unambiguously show that (*i*) even if the electrochemical properties of different electrodes are practically identical when assessed by surface insensitive outer sphere redox (OSR) probes their behavior with inner sphere redox (ISR) probes can be drastically different. Further, (*ii*) the choice of the modification method (structural, chemical, electrochemical) heavily depends on nature of the target analyte, which are typically ISR probes. Although, (*iii*) chemical changes in the carbon phase appeared to be minor, effects of different treatments on oxidation states of Fe appeared to have a strong effect on the electrochemical performance of the networks in the case of ISR probes.

1. Introduction

Since carbon nanotubes (CNTs) were discovered in 1991 [1], this class of nanomaterials has been extensively investigated for various applications [2] owing to their unique material properties [3–5]. Different kind of configurations containing multi-walled (MWCNT) or single-walled carbon nanotubes (SWCNTs) have been realized, including also SWCNT networks [6]. The latter materials are especially attractive from the electroanalytical point of view as it is possibly to heavily modify them both (*i*) structurally and (*ii*) chemically with different treatments. The feasible material properties of CNTs has led to their wide use particularly in the field of electroanalytical applications, where they have been extensively used in the detection of different (bio) molecules [7–10]. However, despite the large number of applied research, the published electroanalytical studies frequently lack consistent characterization of physicochemical properties of CNTs [11–13]. As CNTs performance heavily depend on the synthesis parameters as well as the possible purification/modification steps often used to remove residual metal catalyst particles and amorphous carbonaceous impurities [5,14], without in depth structural knowledge about them, discovering any structure-property associations for these materials becomes extremely difficult. As electrochemical performance of a carbon electrodes is affected by numerous factors including microstructure, surface cleanliness and surface chemistry [15], it can be expected that CNTs fabricated under different conditions can show a wide spectrum of electrochemical properties. This is especially true in detection of inner-sphere (ISR) analytes, which are sensitive to the reactive sites at the electrode surface such as surface oxides [16–18] and defects [19]. These issues have been recently discussed in detail in a comprehensive investigation of structure property relationships in carbon electrochemistry [20].

Here, we use our previously extensively characterized system, namely SWCNT networks [20–23]. We investigate the effects of (*i*) structural and (*ii*) chemical modifications on the electrochemical

* Corresponding author at: Department of Electrical Engineering and Automation, School of Electrical Engineering, Aalto University, PO Box 13500, 00076 Aalto, Finland.
E-mail address: tomi.laurila@aalto.fi (T. Laurila).

https://doi.org/10.1016/j.electacta.2023.143059
Received 18 May 2023; Received in revised form 11 August 2023; Accepted 19 August 2023
Available online 20 August 2023

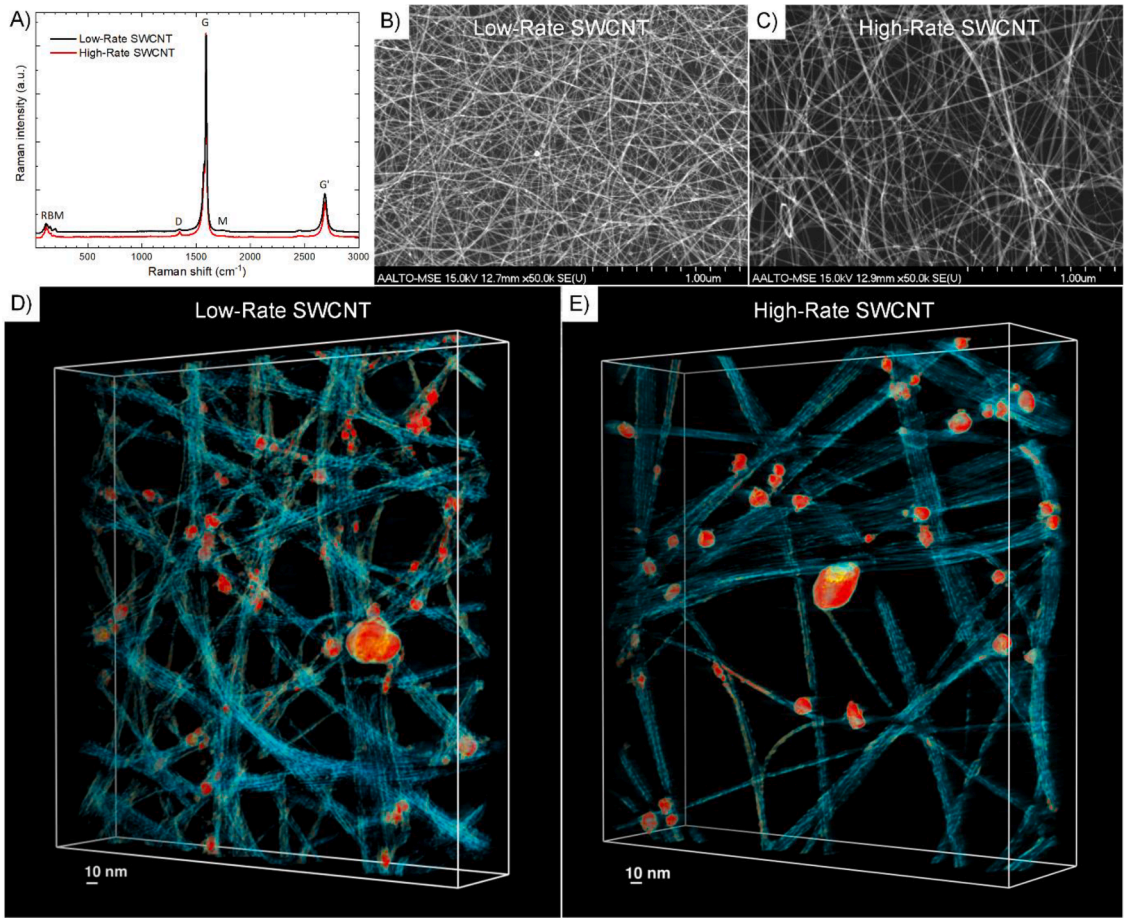

Fig. 1. A) Raman spectra normalized to G peak intensity and offset for clarity. SEM micrographs from non-densified self-standing films and the TEM 3D reconstructions illustrating the structure of pristine B,D) Low-Rate and C,E) High-Rate SWCNT networks. Reprinted from Leppänen et al. [22].

Table 1
Characterization results from pristine Low- and High-Rate SWCNT networks. Reproduced from Leppänen et al. [22].

Sample	Sheet resistance (Ω/sq) $N = 10$	Raman I_D / I_G $N = 3$	SEM Open/Close – ratio $N = 5$
Low-Rate	244 ± 20	0.002 ± 0.000	0.14 ± 0.02
High-Rate	218 ± 16	0.009 ± 0.003	0.34 ± 0.04

properties of these materials. To systematically assess the structure-property associations, we start by providing in depth analyses of the physical and chemical properties of the SWCNT networks and how these are affected by the different treatments. Then we proceed to investigate the electrochemical properties of the materials and especially how the different treatments have affected them. To have a consistent step by step approach to this complex problem, we start with $Ru(NH_3)_6^{2+/3+}$ and $IrCl_6^{3-/2-}$ redox probes known to be true outer sphere redox (OSR) probes insensitive to any surface chemical features of the electrodes. In the next step, we use $Fe^{2+/3+}$ redox species known to be sensitive to oxygen functionalities present on the surface. Finally, we proceed to the most complex problem of true inner sphere redox probes and use dopamine (DA) as our probe molecule to assess the full complexity of chemical effects on the electrochemical kinetics.

By using the above stated systematic approach we can show that (*i*) even rather drastic geometrical changes of the networks did not induce significant effects on the electrochemical properties. (*ii*) Electrochemical oxidation slightly increased the number of oxygen functionalities in the network and especially affected the oxidation state of Fe present in the SWCNT networks somewhat favoring the formation of more oxygen rich oxides. (*iii*) Nitric acid treatment on the other hand did not favor similar formation of oxygen rich Fe oxides, as its X-ray absorption spectroscopy (XAS) spectra resembled closely that of the pristine SWCNTs. Instead, some cleaning effect and subsequent increase in the electrochemically active surface area (ECAS) was observed in comparison to pristine SWCNTs based on the electrochemical data. (*iv*) These two different effects on type of Fe-oxides were highlighted in the opposite trends seen with two different ISR redox probes, namely $Fe^{2+/3+}$ and DA. In the case of the former probe, the electrochemically treated networks exhibited fastest kinetics whereas in the case of DA the HNO_3 treated, and the pristine ones were clearly faster. These results show that (*i*) even if the electrochemical properties of different electrodes are practically identical when assessed by OSR probes their behavior with ISR probes may be drastically different. Further, (*ii*) the choice of modification method heavily depends on the target analyte (ISR probe). Finally, (*iii*) even though chemical changes in the carbon phase after the various treatments were very minor, the changes in the oxidation state of iron nanoparticles appeared to have a strong effect on the electrochemical properties of the SWCNT networks.

2. Experimental

The SWCNT network fabrication, transmission electron microscopy (TEM) tomography, scanning electron microscopy (SEM), conductive atomic force microscopy (PeakForce Tunneling AFM, PF-TUNA) and Raman spectroscopy are described in more detail in [22] and thus, only brief description is provided here.

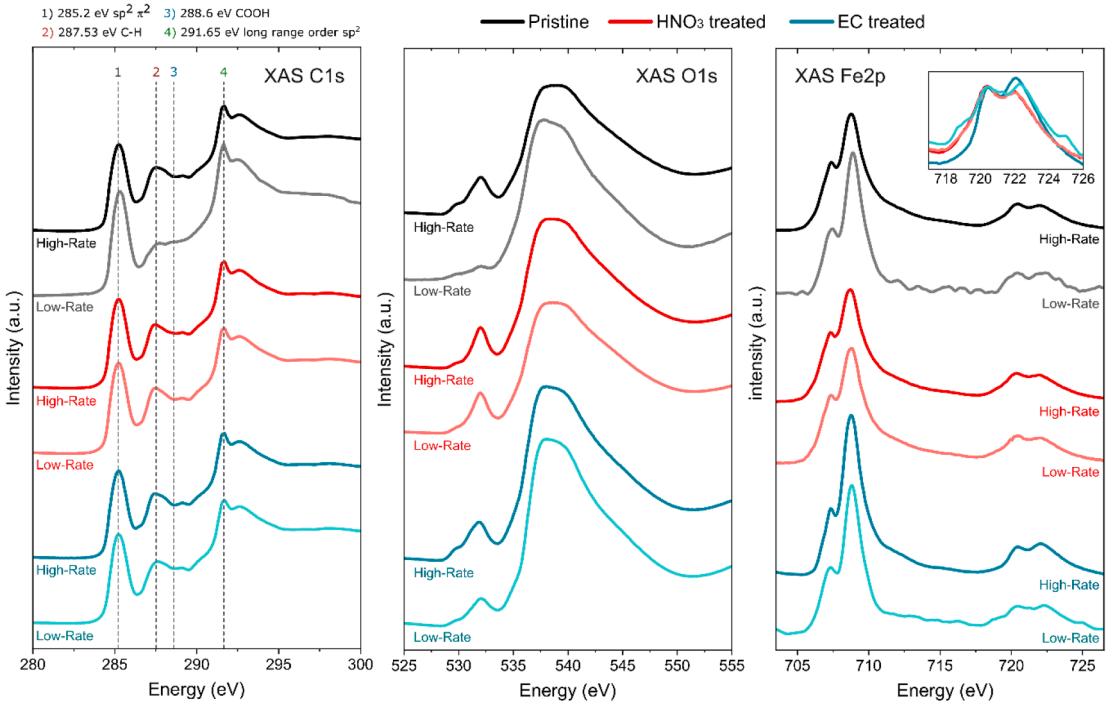

Fig. 2. XAS C1s, O1s and Fe2p spectra of investigated SWCNT networks. C1s and Fe2p spectra are normalized, whereas O1s presents the absolute intensity. The inset in Fe2p spectra shows a magnification of the double peak at higher energy for HNO_3 and EC treated SWCNTs.

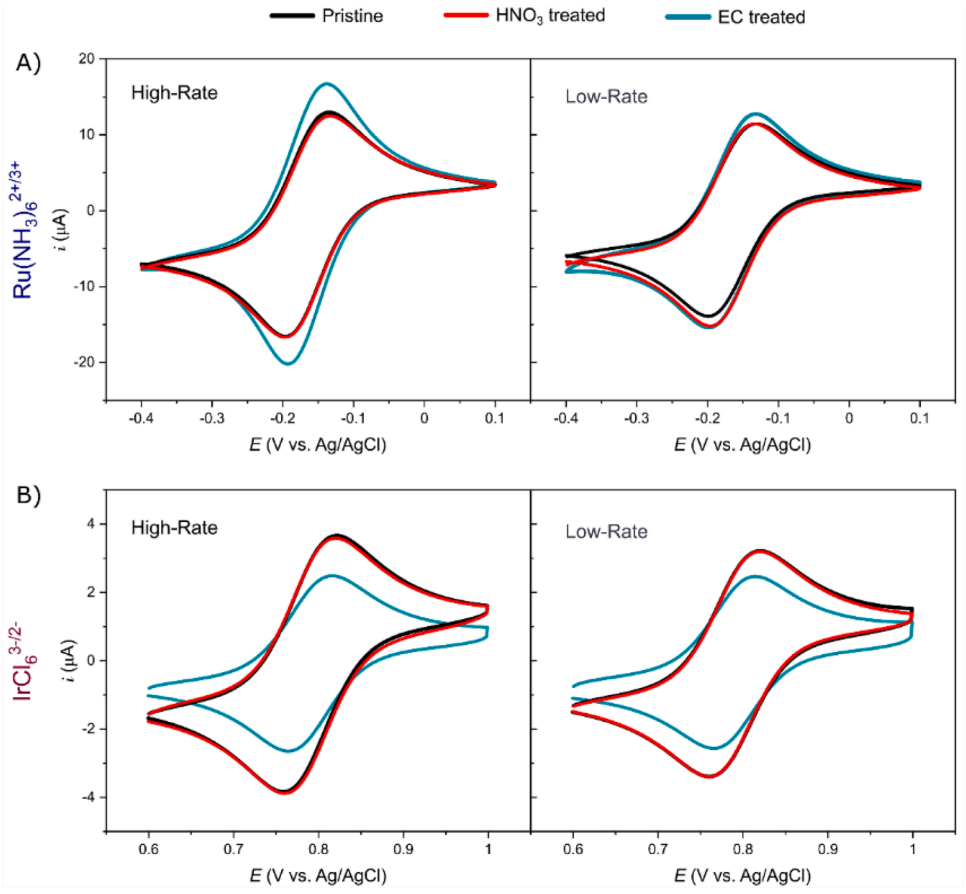

Fig. 3. Cyclic voltammograms of the Low- and High-Rate SWCNT networks in A) $Ru(NH_3)_6^{2+/3+}$ and B) $IrCl_6^{3-/2-}$ in 1 M KCl with scan rate 100 mV/s.

Table 2
Results of the cyclic voltammetry measurements in $Ru(NH_3)_6^{2+/3+}$ and $IrCl_6^{3-/2-}$. The standard heterogenous rate constant k^0 was calculated with Nicholson method [39], whereas the kinetic parameter Λ with method proposed by Matsuda and Ayabe [40]. Electrochemically active surface area was obtained with Randles-Ševčík equation from $Ru(NH_3)_6^{2+/3+}$ $i_{p,a}$. Diffusion coefficients used to evaluate k^0, Λ and A_{eff} were taken from [41,42]. For all the tabulated values $N = 3$.

Electrode		$Ru(NH_3)_6^{2+/3+}$						$IrCl_6^{3-/2-}$						
		ΔE_p (mV)	$i_{p,a}$ (μA)	$i_{p,c}$ (μA)	$i_{p,a}$ / $i_{p,c}$	k^0 (cm·s^{-1})·10^{-2}	Λ	log-plot slope	ΔE_p (mV)	$i_{p,a}$ (μA)	$i_{p,c}$ (μA)	$i_{p,a}$ / $i_{p,c}$	k^0 (cm·s^{-1})·10^{-2}	Λ	log-plot slope	A_{eff} (cm^2) 0.10^{-2}
High-Rate	Pristine	63 ± 3	15.7 ± 1.1	17.0 ± 1.2	0.93 ± 0.01	10.9 ± 8.6	22 ± 7	0.48	63 ± 3	3.7 ± 0.1	3.8 ± 0.2	0.99 ± 0.01	12.3 ± 8.2	23 ± 16	0.47	6.61 ± 0.46
	HNO_3 treated	64 ± 2	14.5 ± 0.4	16.0 ± 0.6	0.91 ± 0.02	7.8 ± 5.3	16 ± 10	0.48	59 ± 5	3.9 ± 0.6	4.0 ± 0.6	0.98 ± 0.02	23.4 ± 16.0	44 ± 30	0.47	6.11 ± 0.17
	EC treated	55 ± 6	17.6 ± 2.5	19.5 ± 2.8	0.90 ± 0.01	31.9 ± 14.8	64 ± 29	0.54	52 ± 4	2.2 ± 0.3	2.2 ± 0.3	0.96 ± 0.02	41.8 ± 9.4	79 ± 18	0.52	7.42 ± 1.05
Low-Rate	Pristine	69 ± 2	13.7 ± 0.1	14.8 ± 0.2	0.92 ± 0.02	2.3 ± 0.4	4 ± 1	0.45	61 ± 1	3.4 ± 0.1	3.3 ± 0.1	1.01 ± 0.02	16.9 ± 4.0	32 ± 8	0.48	5.77 ± 0.04
	HNO_3 treated	64 ± 2	14.2 ± 0.2	15.4 ± 0.2	0.92 ± 0.01	6.2 ± 3.6	12 ± 7	0.48	61 ± 2	3.5 ± 0.1	3.5 ± 0.1	0.99 ± 0	17.8 ± 5.7	34 ± 11	0.47	5.98 ± 0.08
	EC treated	69 ± 6	14.8 ± 1.5	16.1 ± 2.6	0.93 ± 0.08	3.2 ± 2.1	6 ± 4	0.49	50 ± 2	2.1 ± 0.1	2.2 ± 0.1	0.96 ± 0.03	48.9 ± 4.3	93 ± 8	0.56	6.24 ± 0.63

2.1. SWCNT network fabrication

Single-walled carbon nanotube networks were fabricated by Canatu Oy using a high-temperature floating catalyst chemical vapor deposition in laminar flow reactor. Growth was carried out in carbon monoxide atmosphere. Fe particles decomposed from a ferrocene precursor were used as a catalyst for the growth of SWCNTs. More detailed information about the fabrication process can be found from Kaskela et al. [6], Moisala et al. [24].

In this study, two different types of SWCNT networks were investigated. The networks were synthesized at different collection rates of 100% and 500%, respectively, by adjusting the amount of ferrocene in the gas phase. The amount of iron was regulated by changing the temperature of the ferrocene cartridge, which influenced the vapor pressure of ferrocene. Collection time was adjusted accordingly, based on in-situ optical rate absorbance monitoring, to obtain networks with the same thickness. The sample obtained with a slower collection rate was identified as Low-Rate SWCNT, while the one obtained at a rate of 500% was identified as High-Rate SWCNT.

2.2. Transmission electron microscope tomography

JEM-2800 electron microscope (JEOL) was used for collecting TEM micrographs. SWCNT networks were directly press-transferred on EM gold (Au) 100×400-mesh-MultiA-holey-carbon grids (Quantifoil). Tilt-series of TEM micrographs was collected at 80 kV RECORDER application (TEMography) with following settings: Goniometer tilts spanning −72 to +72°, increment steps 2°, CCD (GATAN), ORIUS SC200, 2048×2048 camera, pixel X,Y scale 0.262017 nm, at magnification of 400 k.

Tilt-series were saved as stacks.mrc in 16bit format and converted to 32bit stacks.mrc using e2projectmanager.py, GUI application (EMAN2).

The 32bit stacks.mrc were aligned using ETOMO, GUI application (IMOD). Briefly, automatic coarse cross-correlation alignment, followed additional fine alignment using the patch-tracking method.

For tomography, maximum entropy method (MEM) [25,26] was used for 3D reconstruction of aligned.ali stacks. Before running tomography, aligned.ali stacks were 2 x binned and ROI cropped with scripts initiated in the Aalto Nanomicroscopy Center laboratory. MEM-3D-reconstruction volumes produced were visualized and scrutinized, in stereo mode, using UCSF CHIMERA application. Programs were all run in Mac Pro, Cylinder model, Twelve Core (64 GB).

2.3. Scanning electron microscopy

Hitachi S-4700 SEM at 15 kV accelerating voltage was used for imaging self-standing SWCNT networks. Open-to-close ratios were computed from SEM images by gray-scale thresholding to binary color in Image J.

2.4. X-ray absorption spectroscopy

Soft XAS measurements were performed on the 33-pole wiggler beamline 10–1 at Stanford Synchrotron Radiation Lightsource (SSRL) using 55° incidence angle (magic angle) of X-rays. A resolution of ~200 meV was achieved with a spherical grating monochromator which was operated using 40 × 40 μm slits. X-ray beam spot size was approximately 1 × 1 mm2 with total flux in order of 10^11 photons/sec. The X-ray energy for iron 2p edge was measured from 695 eV to 735 eV, whereas for carbon and oxygen 1 s edge were from 260 eV to 340 eV and 520 eV to 560 eV, respectively. A Keithley picoammeter was used for amplifying the drain current to collect all the data in total electron yield (TEY) mode, where the incoming flux was measured using a nickel grid coated with Au sputtered film. Here, a reference sample was used for energy calibration of the data prior to the data analysis. The C 1s spectra were confirmed to match their energy calibration by observing the core-

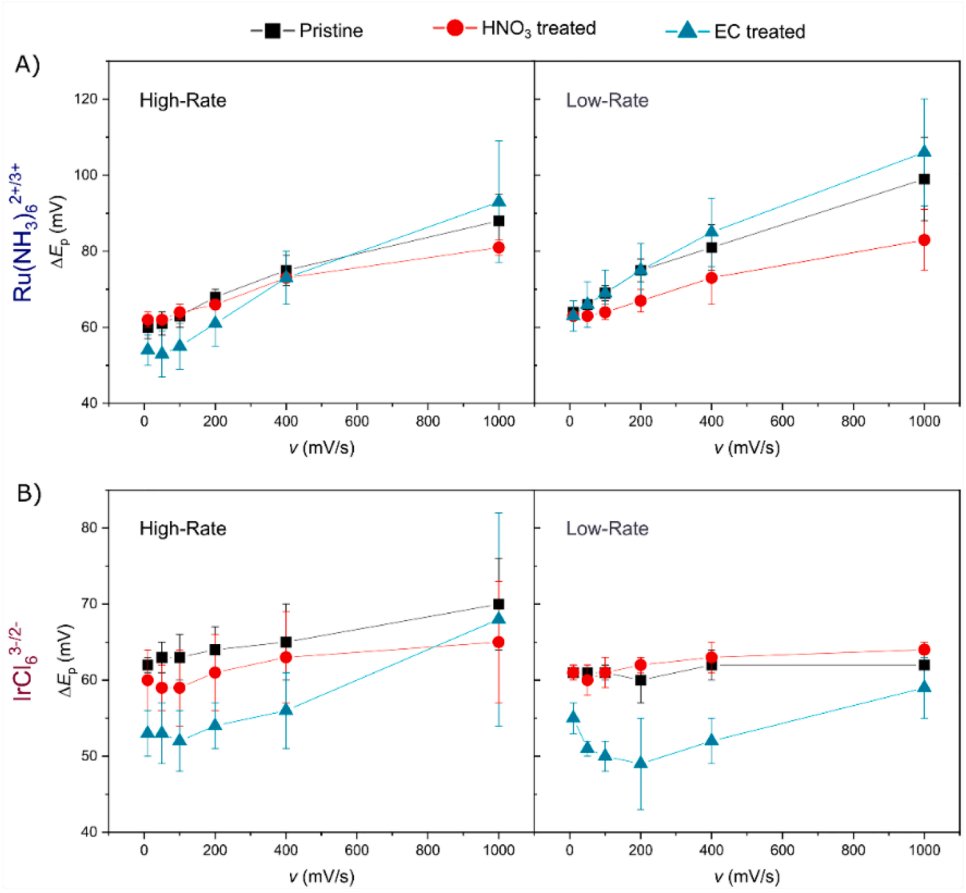

Fig. 4. The peak-to-peak separation as function of scan rate observed in A) $Ru(NH_3)_6^{2+/3+}$ and B) $IrCl_6^{3-/2-}$.

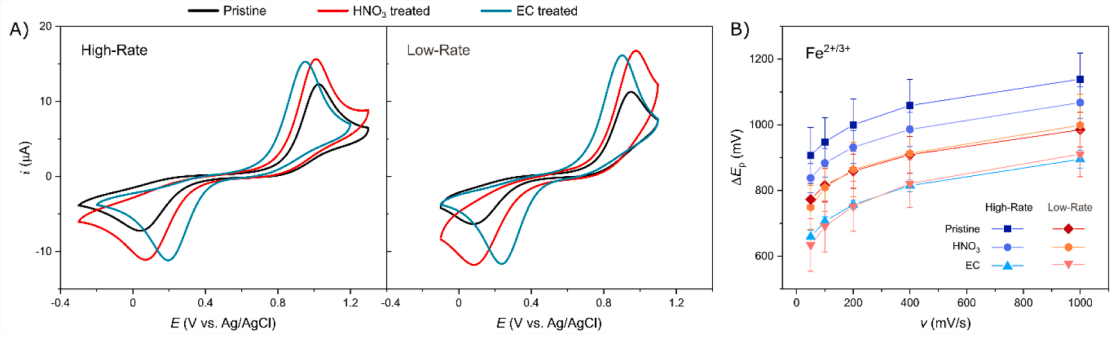

Fig. 5. A) Cyclic voltammograms of the SWCNT networks in $Fe^{2+/3+}$ with scan rate of 200 mV/s and B) observed $\triangle E_p$ as function of scan rate.

exciton signature at 291.65 eV [26–28] after the reference sample energy alignment. The presented C 1s and Fe 2p spectra are normalized, where the Fe 2p spectra were energy aligned to match metallic iron signature at 707.36 eV [27]. Beamline energy calibration is based on matching the Ni L3 in 2nd order at 426.35 eV prior to measurement for low energy samples (up to O1s) and Ni L3 at 852.7 eV for high energy samples (above O1s). The presented C 1s, Fe 2p and O 1s spectra in Fig. 2 shows the average value from three different locations. Furthermore, all the data treatment (background subtraction and energy correction) was done using IGOR Pro v. 8.02 software.

2.5. Raman spectroscopy

Raman spectroscopy was performed by a Horiba Jobin-Yvon Labram HR confocal Raman system with an 488 nm argon laser with 10 mW power on sample. Spot size of 1 μm was used with an Olympus 100× objective. Spectra were acquired in the range of 50 to 3000 cm^{-1} with a 600 lines/inch diffraction grating, exposure time of 15 s, and accumulation averaging count of two. Spectroscopic calibration was performed on intrinsic Si wafer (Ultrasil). Spectra were fitted by one Lorentzian peak for D-band, and two Lorentzian peaks for the G-band (G^+ and G^-), to obtain the I_D/I_G peak intensity ratios, as explained in literature [28].

2.6. Electrochemical measurements

Cyclic voltammetry experiments were carried out with Gamry Reference 600+ potentiostat in a three-electrode cell. Pt wire (Goodfellow) was used as a counter electrode, Ag/AgCl (+0.199 V vs. SHE, Radiometer analytical) as a reference electrode and SWCNT networks investigated here as a working electrode. Detailed description of SWCNT

Table 3
The peak-to-peak separation, onset potential and peak current ration obtained in $Fe^{2+/3+}$ with scan rates of 100 and 1000 mV/s ($N = 3$).

Electrode		ν = 100 mV/s			ν = 1000 mV/s		
		ΔE_p (mV)	E_{onset} (mV)	$i_{p,a}$ / $i_{p,c}$	ΔE_p (mV)	E_{onset} (mV)	$i_{p,a}$ / $i_{p,c}$
High-Rate	Pristine	948 ± 74	826 ± 34	1.8 ± 0.1	1139 ± 80	889 ± 33	2.5 ± 0.2
	HNO_3 treated	884 ± 44	802 ± 18	1.5 ± 0.1	1068 ± 48	870 ± 20	1.6 ± 0.0
	EC treated	706 ± 14	734 ± 16	1.3 ± 0.0	895 ± 27	813 ± 20	1.5 ± 0.1
Low-Rate	Pristine	816 ± 51	735 ± 25	1.8 ± 0.1	985 ± 53	786 ± 21	1.9 ± 0.1
	HNO_3 treated	809 ± 73	738 ± 33	1.4 ± 0.1	999 ± 95	809 ± 39	1.5 ± 0.1
	EC treated	691 ± 78	730 ± 35	1.5 ± 0.1	911 ± 69	823 ± 41	1.7 ± 0.3

preparation can from Leppänen et al. [21]. Briefly, SWCNT electrodes prepared by press-transferring a smaller piece of network onto a glass substrate (Thermo Scientific, ISO 8037/I) and densified with a drop of 99.5 wt-% ethanol (Altia). Electrical contact was painted with conductive silver paint (Electrolube). The working area of the SWCNT network was defined by covering the surface with inert PTFE-tape (Saint-Gobain Performance Plastics CHR 2255-2) with a 3 mm hole.

Electrochemical measurements were conducted for three different types of Low- and High-Rate SWCNT networks: (*i*) pristine (as-prepared), (*ii*) HNO_3 treated and (*iii*) electrochemically (EC) treated equaling into total of six (6) different sample types. 15 min HNO_3 treatment was carried out by drop-casting 10 M HNO_3 on top of the prepared SWCNT electrode, whereas electrochemical oxidation was conducted in 10 mM phosphate-buffered saline (PBS, pH 7.4) by holding the electrode at 1.3 V (vs. Ag/AgCl) for 5 min.

The CV measurements were carried out in 1 mM $Ru(NH_3)_6^{2+/3+}$, 1 mM $IrCl_6^{3-/2-}$, 1 mM $Fe^{2+/3+}$ and 100 µM DA. Solution were prepared from following chemicals purchased from Sigma-Aldrich: hexaaminerruthenium(III) chloride, potassium hexachloroiridate(IV), iron(II) sulfate hexahydrate and dopamine hydrochloride. $Ru(NH_3)_6^{2+/3+}$ and $IrCl_6^{3-/2-}$ were dissolved in 1 M KCl (Merck Suprapur, pH 6.8), where as $Fe^{2+/3+}$ in 0.2 M $HClO_4$ (VWR Chemicals, pH 1) and DA in 10 mM PBS. In case of DA, PBS was purged with N_2 for 30 min prior to the experiment.

All measurements were repeated at least three times with different electrodes. In addition, all measurements were carried out at room temperature inside a Faraday's cage.

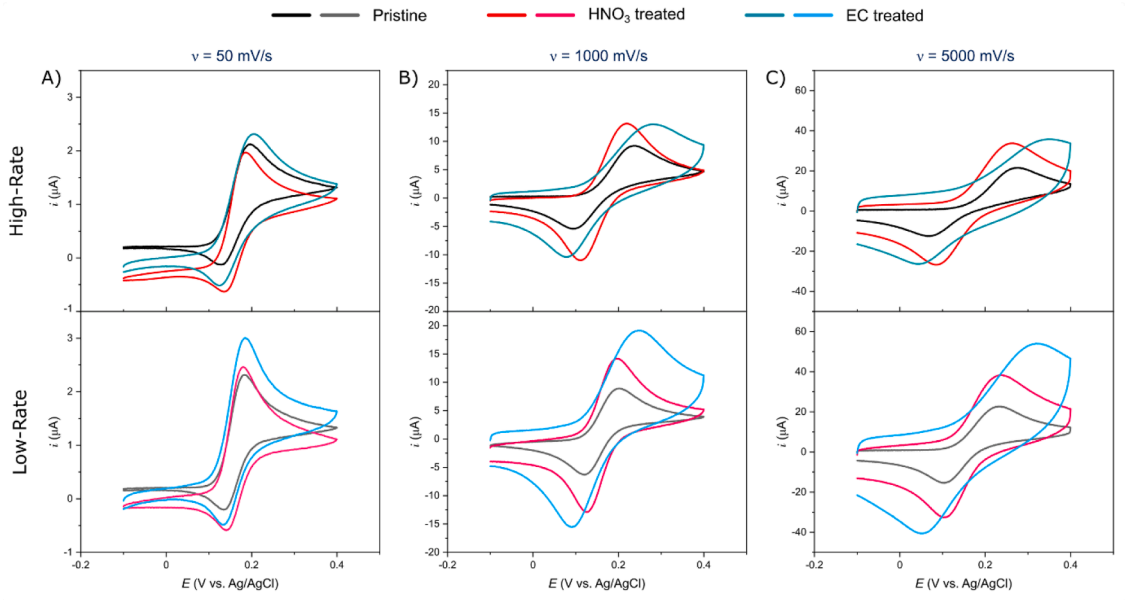

Fig. 6. Cyclic voltammograms of the Low- and High-Rate networks in 100 µM dopamine in PBS with scan rates A) 50 mV/s, B) 1000 mV/s and B) 5000 mV/s.

Table 4
The results obtained from the cyclic voltammetry measurements in 100 µM dopamine in PBS with scan rates of 50 mV/s and 5000 mV/s ($N = 3$).

Electrode		ν = 50 mV/s						ν = 5000 mV/s						
		ΔE_p (mV)	$E_{p,a}$ (mV)	$E_{p,c}$ (mV)	E_{onset} (mV)	$i_{p,a}$ (µA)	$i_{p,a}$ / $i_{p,c}$	ΔE_p (mV)	$E_{p,a}$ (mV)	$E_{p,c}$ (mV)	E_{onset} (mV)	$i_{p,a}$ (µA)	$i_{p,a}$ / $i_{p,c}$	log-plot slope
High-Rate	Pristine	74 ± 15	200 ± 9	126 ± 6	125 ± 2	1.8 ± 0.2	1.7 ± 0.2	216 ± 34	280 ± 22	64 ± 6	161 ± 12	14.7 ± 2.3	1.8 ± 0.4	0.42
	HNO_3 treated	58 ± 17	191 ± 12	134 ± 6	124 ± 1	2.1 ± 0.3	1.8 ± 0	167 ± 61	256 ± 35	134 ± 6	145 ± 24	22 ± 0.3	1.3 ± 0.2	0.51
	EC treated	82 ± 10	206 ± 8	125 ± 2	121 ± 1	2.4 ± 0.2	2.7 ± 0.7	295 ± 7	339 ± 6	44 ± 2	162 ± 4	18 ± 5.1	1.7 ± 0.3	0.45
Low-Rate	Pristine	58 ± 18	190 ± 12	132 ± 6	124 ± 2	2 ± 0.1	1.8 ± 0.1	154 ± 44	248 ± 26	93 ± 18	133 ± 14	18 ± 2.3	1.2 ± 0.1	0.48
	HNO_3 treated	42 ± 5	182 ± 2	140 ± 4	124 ± 1	2.2 ± 0.1	1.7 ± 0	114 ± 37	224 ± 20	110 ± 17	128 ± 1	27.9 ± 6.7	1.1 ± 0	0.56
	EC treated	52 ± 6	185 ± 4	134 ± 2	119 ± 1	2.5 ± 0.4	2.0 ± 0.1	258 ± 8	312 ± 6	54 ± 2	140 ± 3	24 ± 8.4	1.4 ± 0.3	0.49

3. Results and discussion

3.1. Physical and chemical characterization

Two SWCNT networks of the same optical transmittance were collected at widely different rates by varying the ferrocene cartridge temperature as discussed in more detail in [22]. The I_D/I_G ratios as fitted from the Raman spectra given in Fig. 1A, showed a small increase in the number of defects when moving from the low-rate to the high-rate SWCNTs. However, these values were still very low, indicating highly defect free tubes in both cases [28]. Further, the two samples exhibited similar sheet resistance values as well as comparable PF-TUNA conductivities [22] indicating that the electrical properties of the two types of structurally different networks were alike. As a note, the sheet resistance technique measures the resistance between opposite sides of a square of a material, whereas the PF-TUNA mainly probes the *z*-axis conductivity through the network. From the electrochemical application point of view, the latter property is much more important.

Low magnification SEM images showing the overall network structure are exhibited in Fig. 1B and C. Open-to-close -ratios of the CNT networks were calculated by grayscale to binary conversion from SEM images to assess the network density. The obtained values are included in Table 1.

The three-dimensional reconstructions for both pristine SWCNT networks based on the TEM tomography technique are presented in Fig. 1D and E. From the figures it is clearly seen that in both networks the SWCNTs exist mainly in bundles and not as an individual tubes. Further observations include the following: (*i*) high-rate SWCNT sample network appears overall less dense and (*ii*) the average size of the bundles seems to be significantly larger in the case of high-rate sample than in the low-rate one. Quantitative analyses from the XPS revealed that the content of Fe was identical in both networks [22].

Analysis of the surface chemistry of the geometrically different samples was carried out by measuring C 1s, Fe 2p and O 1s spectra with XAS (Fig. 2). No marked differences were observed between the pristine SWCNT samples. However, based on the XAS Fe 2p spectra a small but clear difference was observed in the composition of iron between the two types of networks. With pristine Low-Rate network the intensity of peak ~709 eV is higher in comparison to High-Rate which indicated that the former contains slightly more oxidized phases of iron, presumably, Fe_3O_4 and Fe_2O_4 [29–31]. These oxides have considerably higher intensity than the metallic iron at 707.36 eV [27,32]. However, the relative intensities of the two peaks around 720–723 eV indicate that there could also be some contribution from lower iron oxides (FeO) in this case [31,33]. As metallic iron may be masked by oxidized iron, it is very likely that the signal is combination of all these phases.

Next the surface chemistry of electrochemically and nitric acid treated networks was assessed. The following main results were obtained. Based on the C1s and O1s spectra neither the electrochemical nor nitric acid treatment induced marked changes in the surface chemistry of carbon phase. Due to the high reactivity of SWCNT networks towards atmospheric impurities such as oxygen and hydrogen, the age of the sample can have a slight impact on the observed surface chemistry. This phenomenon is also evident in the subtle variations observed between Low-Rate and High-Rate SWCNT networks. Therefore, it is important to acknowledge that minor changes in the surface chemistries of carbonaceous samples should not be given significant consideration unless the sample ages are identical.

On the Fe 2p spectra, small but still clear differences were seen in the chemical states of Fe after the two treatments. Intensity of the iron oxide peak enhanced significantly when the SWCNTs were electrochemically pretreated. Based on the extensive literature survey [27,29–31,34,35], Fe 2p spectrum of the EC treated is similar to Fe_2O_3 with separate and well-defined peak at lower energy. We suggest that Fe 2p spectrum for the EC treated arise from phases of metallic Fe, Fe_3O_4 and Fe_2O_3. Additionally, it is very likely that some carbon is dissolved into the iron as well [32,36]. In the double peak region (around 722 eV) one can now observe that the intensities of the two peaks are different when compared to pristine sample, which indicates less contribution from oxygen poor oxides relative to the oxygen rich oxides [31,33]. The HNO_3 treated sample resembles chemically the pristine samples more than the electrochemically treated ones. Especially, within the double peak region (722 eV) the ordering of the intensities is similar to pristine SWCNT. Thus, based on the XAS the main differences between the different SWCNT networks are in the nature of the iron oxides – more oxygen rich Fe-oxides are present in electrochemically treated SWCNTs. This highlights that the main effects of the treatments are not found in the carbon phase, but instead in the oxidation states of Fe. Finally, we note that in all spectra (pristine, electrochemically and HNO_3 treated) the $sp^2\,\pi^*$ peak at 285.2 eV and the exciton peak at 291.65 eV stays well defined providing evidence that CNT long range ordering is well preserved in all cases.

3.2. Electrochemical characterization

Effects of structural differences and chemical treatments on the charge transfer properties were characterized by using $Ru(NH_3)_6^{2+/3+}$ and $IrCl_6^{3-/2-}$ species. Cyclic voltammograms are shown in Fig. 3. These two species are known true outer sphere redox probes that can be utilized to probe the electronic properties (surface density of states (DOS)) of the electrode materials in the absence of additional chemical complications. Note also that the two probes have very different charges and formal potentials enabling one to assess possible electrostatic effects as well. No changes in the peak positions that would indicate significant differences in surface DOS were seen as expected based on the practically identical electrical properties (Table 2). In addition, the geometrical features of the networks did not induce any notable thin liquid layer effects within the scan range region investigated except the small drop in the peak-to-peak separation, ΔE_p, values with the electrochemically treated networks in the scan rate range of 100–400 mV/s with $IrCl_6^{3-/2-}$ probe (see Fig. 4). The absence of notable thin liquid layer formation is most likely caused by the mismatch in the diffusion layer thickness and the network dimensions [37].

When the oxidation peak currents for the two reactions are compared, it is clear that $Ru(NH_3)_6^{2+/3+}$ shows in all cases higher currents than $IrCl_6^{3-/2-}$ despite the equal concentrations and number of electrons ($n = 1$ in both cases) transferred. This can be rationalized by considering how different the electrode surfaces are around the formal potentials of the two probes. (*i*) Network will be negatively charged around the formal potential of the $Ru(NH_3)_6^{2+/3+}$ reaction whereas the opposite is true for $IrCl_6^{3-/2-}$ reaction as the point of zero total charge (pztc) is between the two formal potentials [20]. In addition, the pztc of the SWCNT network is closer to the formal potential of $Ru(NH_3)_6^{2+/3+}$ than that of $IrCl_6^{3-/2-}$ [20] resulting into a higher charge density on the surface in the latter case. This leads to (*ii*) the presence of less ordered water at a potential range for the formal potential of the $Ru(NH_3)_6^{2+/3+}$ reaction and a relatively more compact water layer for the potential range corresponding to the $IrCl^{3-/2-}$ reaction. Further, since the carbon phase of the SWCNT network is positively charged around the formal potential of $IrCl_6^{3-/2-}$, (*ii*) stronger adsorption of ions (anions) can shift the outer Helmholtz plane further into the solution at these adsorption sites. This will further lead to (*iii*) lowering of the analyte concentration within the effective electron transfer distance from the surface, as some of the $IrCl_6^{3-/2-}$ probes will stay further away from the electrode surface, therefore having weaker electronic coupling and thus lower probability for electron transfer [38].The overall result from (*i*) – (*iii*) would be (*iv*) a decrease in the measured peak current for the $IrCl_6^{3-/2-}$ reaction in comparison to the $Ru(NH_3)_6^{2+/3+}$ reaction, as observed.

Interestingly, the electrochemical oxidation of the SWCNT network seems to further increase the difference between the currents measured for the two probes. In fact, the $IrCl_6^{3-/2-}$ reaction on the electrochemically treated electrodes is the most reversible, but still shows the lowest

currents, whereas the pristine and HNO_3 treated electrodes appear to behave practically identically. These differences can be caused by the fact that there is higher number of oxygen rich Fe-oxide species on the surface of the electrodes after the electrochemical treatment in comparison to other SWCNT networks, as this is known to affect the location of the pztc [43]. However, further investigations are needed to clarify this issue. Oxidation to reduction peak current ratios were observed to be slightly less than one with $Ru(NH_3)_6^{2+/3+}$, which may indicate weak physisorption of the oxidized species. On the other hand, redox reactions of $IrCl_6^{3-/2-}$ did not show any indication of adsorption interactions as the current ratio was very close to 1 with all the electrodes.

Next, we moved on to a slightly more complex redox probe $Fe^{2+/3+}$ of which reaction kinetics is known to be sensitive to oxygen functionalities present on the electrode surface [16,18]. Results are presented in Fig. 5 and Table 3. As expected, the EC-oxidation treatment improved the kinetics of the $Fe^{2+/3+}$ reaction, which is consistent with the spectroscopy results showing that there were more oxygen rich Fe-oxide species on its surface in comparison to the other types of samples. The HNO_3 treated and the pristine SWCNT networks were electrochemically practically the same (peak potentials were almost identical), but the HNO_3 treated network had a bit higher peak current. This suggests that the HNO_3 treatment somewhat increased the ECAS. Additionally, Raman spectroscopy data revealed an increase in the intensity of the G peak, providing further evidence to support the claim that HNO_3 treatments increase electrochemically active surface area (see supporting information, Figure S1). Low-rate networks showed in general faster kinetics than the high-rate ones, despite the exact nature of the treatment utilized. One reason for this difference is anticipated to be denser network structure and smaller bundle size (as shown in Fig. 1D and E) that should further increase the ECAS inside the SWCNT network.

Finally, we moved on to a true inner sphere redox system dopamine to investigate the surface chemical effects on the reaction kinetics. The results are shown in Fig. 6 and Table 4. At low scan rates the reaction rates appeared to be almost the same with HNO_3 treated and pristine ones being the fastest. However, as a function of increasing scan rate, the differences started to magnify, HNO_3 being the fastest, then the pristine network almost as fast and finally the electrochemically treated network clearly as the slowest. The difference between the two treatments (HNO_3 and electrochemical oxidation) can be rationalized in the following way. Based on the XAS results it appears that the Fe oxides are less oxygen rich in the case of HNO_3 treated and pristine SWCNT than in electrochemically treated network. It is known that when one moves to more oxygen rich metal oxides [44], the IP and thus pKa decrease and subsequently the acidity of the oxide surfaces increase. Therefore, one can conclude that the surface of the HNO_3 treated network (as well as pristine) should be a better hydrogen bond acceptor (less acidic) than the electrochemically treated one with its oxygen rich more acidic oxides [45]. This could facilitate the proton transfer reaction associated with the DA oxidation reaction [46] on the surface of the HNO_3 treated networks with respect to other types of networks and thus increase the overall rate of reaction. The influence of the oxidation state of Fe is also supported by the results of Raman spectroscopy (see Figure S1 in the supplementary material), which indicated an increase in the number of defects in the EC-treated network, compared to both the HNO3-treated and pristine networks. However, even with the increase in defects, the EC network still exhibited the slowest overall reaction rate.

From the structural point of view, the low iron SWCNTs appeared to be slightly better than high iron ones in all cases. This is likely caused by (*i*) higher number of Fe (oxide) particles with smaller size in the case of low rate SWCNTs and (*ii*) slightly denser network leading into higher reactive site density. Peak potentials for the oxidation of low Fe were also consistently slightly less anodic than those of high Fe. Also, the peak currents were consistently somewhat higher. However, evidence of marked adsorption was not seen with any of the electrode types.

4. Conclusions

We show that (*i*) even rather drastic structural changes of the networks did not induce significant modifications of the electrochemical properties, except the slight differences in the case of ISR probe DA. (*ii*) Electrochemical oxidation somewhat affected the number of oxygen functionalities in the network, but especially it had an effect on the oxidation state of Fe present in the SWCNT networks favoring slightly formation of more oxygen rich oxides. (*iii*) Nitric acid treatment on the other hand did not favor similar formation of oxygen rich Fe oxides, as its XAS spectra resembled closely that of the pristine SWCNTs. Instead, some cleaning effect and subsequent increase in the electrochemically active surface area was observed in comparison to the pristine SWCNTs based on the electrochemical data. (*iv*) These two different effects were highlighted in the opposite trends seen with two different redox probes, namely $Fe^{2+/3+}$ and DA. In the case of the former probe, the electrochemically treated networks exhibited fastest kinetics whereas in the case of DA the HNO_3 treated ones were clearly the fastest closely followed by the pristine SWCNTs. The reason for this difference was anticipated to be the presence of less oxygen rich oxides on HNO_3 treated surface facilitating the proton transfer reaction associated with DA oxidation. These results clearly show that (*i*) even if the electrochemical properties of different electrodes are practically identical when assessed with the OSR probes, their behavior with the ISR probes may be drastically different. Further, (*ii*) the choice of modification method (structural, chemical, electrochemical) heavily depends on the target analyte (ISR probe). (*iii*) Although, chemical changes in the carbon phase very rather minor, the corresponding changes in the oxidation states of Fe appeared to have a strong effect of ISR redox probe kinetics, highlighting once more the importance of metallic catalyst particles in electrochemical properties of carbonaceous nanomaterials. These preliminary results open a new research avenue towards the application specific modification of the SWCNT networks for targeted analytes.

CRediT authorship contribution statement

Elli Leppänen: Investigation, Validation, Formal analysis, Visualization, Writing – original draft, Writing – review & editing. **Eero Gustafsson:** Investigation, Formal analysis. **Niklas Wester:** Resources. **Ilkka Varjos:** Resources. **Sami Sainio:** Investigation, Formal analysis. **Tomi Laurila:** Conceptualization, Writing – original draft, Writing – review & editing, Supervision.

Declaration of Competing Interest

The authors declare that they have no known competing financial interests or personal relationships that could have appeared to influence the work reported in this paper.

Data availability

Data will be made available on request.

Acknowledgments

The authors acknowledge Dr. Pether Engelhard for taking the TEM micrographs and building the 3D reconstruction of SWCNT networks. Mr. Jarkko Etula is acknowledged for taking the SEM images and conducting the Raman spectroscopy experiment.

Supplementary materials

Supplementary material associated with this article can be found, in the online version, at doi:10.1016/j.electacta.2023.143059.

References

[1] S. Iijima, Helical microtubules of graphitic carbon, Nature 354 (1991) 56–58, https://doi.org/10.1038/354056a0.

[2] M.F.L. De Volder, S.H. Tawfick, R.H. Baughman, A.J. Hart, Carbon nanotubes: present and future commercial applications, Science (80-.) 339 (2013) 535–539, https://doi.org/10.1126/science.1222453.

[3] I. Heller, A.M. Janssens, J. Männik, E.D. Minot, S.G. Lemay, C. Dekker, Identifying the mechanism of biosensing with carbon nanotube transistors, Nano Lett. 8 (2008) 591–595, https://doi.org/10.1021/nl072996i.

[4] I. Heller, J. Kong, K.A. Williams, C. Dekker, S.G. Lemay, Electrochemistry at single-walled carbon nanotubes: the role of band structure and quantum capacitance, J. Am. Chem. Soc. 128 (2006) 7353–7359, https://doi.org/10.1021/ja061212k.

[5] T. Laurila, S. Sainio, M.A. Caro, Hybrid carbon based nanomaterials for electrochemical detection of biomolecules, Prog. Mater. Sci. 88 (2017) 499–594, https://doi.org/10.1016/j.pmatsci.2017.04.012.

[6] A. Kaskela, A.G. Nasibulin, M.Y. Timmermans, B. Aitchison, A. Papadimitratos, Y. Tian, Z. Zhu, H. Jiang, D.P. Brown, A. Zakhidov, E.I. Kauppinen, Aerosol-synthesized SWCNT networks with tunable conductivity and transparency by a dry transfer technique, Nano Lett. 10 (2010) 4349–4355, https://doi.org/10.1021/nl101680s.

[7] T. Palomäki, E. Peltola, S. Sainio, N. Wester, O. Pitkänen, K. Kordas, J. Koskinen, T. Laurila, Unmodified and multi-walled carbon nanotube modified tetrahedral amorphous carbon (ta-C) films as in vivo sensor materials for sensitive and selective detection of dopamine, Biosens. Bioelectron. 118 (2018) 23–30, https://doi.org/10.1016/j.bios.2018.07.018.

[8] X.-J. Huang, H.-S. Im, D.-H. Lee, H.-S. Kim, Y.-K. Choi, Ferrocene functionalized single-walled carbon nanotube bundles. Hybrid interdigitated construction film for L-glutamate detection, J. Phys. Chem. C 111 (2007) 1200–1206, https://doi.org/10.1021/jp065747b.

[9] B.E.K. Swamy, B.J. Venton, Carbon nanotube-modified microelectrodes for simultaneous detection of dopamine and serotoninin vivo, Analyst 132 (2007) 876–884, https://doi.org/10.1039/B705552H.

[10] J. Wang, Carbon-nanotube based electrochemical biosensors: a review, Electroanalysis 17 (2005) 7–14, https://doi.org/10.1002/elan.200403113.

[11] K. Wu, J. Fei, S. Hu, Simultaneous determination of dopamine and serotonin on a glassy carbon electrode coated with a film of carbon nanotubes, Anal. Biochem. 318 (2003) 100–106, https://doi.org/10.1016/S0003-2697(03)00174-X.

[12] G. Li, J.M. Liao, G.Q. Hu, N.Z. Ma, P.J. Wu, Study of carbon nanotube modified biosensor for monitoring total cholesterol in blood, Biosens. Bioelectron. 20 (2005) 2140–2144, https://doi.org/10.1016/j.bios.2004.09.005.

[13] M. Zhang, K. Gong, H. Zhang, L. Mao, Layer-by-layer assembled carbon nanotubes for selective determination of dopamine in the presence of ascorbic acid, Biosens. Bioelectron. 20 (2005) 1270–1276, https://doi.org/10.1016/j.bios.2004.04.018.

[14] M. Kumar, A. Yoshinori, Chemical vapor deposition of carbon nanotubes: a review on growth mechanism and mass production, J. Nanosci. Nanotechnol. 10 (2010) 3739–3758, https://doi.org/10.1166/jnn.2010.2939.

[15] R.L. McCreery, Advanced carbon electrode materials for molecular electrochemistry, Chem. Rev. 108 (2008) 2646–2687, https://doi.org/10.1021/cr068076m.

[16] C.A. McDermott, Electron transfer kinetics of aquated Fe[sup +3/+2], Eu[sup +3/+2], and V[sup +3/+2] at carbon electrodes, J. Electrochem. Soc. 140 (1993) 2593, https://doi.org/10.1149/1.2220868.

[17] R.L. McCreery, K.K. Cline, C.A. McDermott, M.T. McDermott, Control of reactivity at carbon electrode surfaces, Colloids Surfaces A Physicochem. Eng. Asp. 93 (1994) 211–219, https://doi.org/10.1016/0927-7757(94)02899-0.

[18] P. Chen, M.A. Fryling, R.L. McCreery, Electron transfer kinetics at modified carbon electrode surfaces: the role of specific surface sites, Anal. Chem. 67 (1995) 3115–3122, https://doi.org/10.1021/ac00114a004.

[19] C.E. Banks, T.J. Davies, G.G. Wildgoose, R.G. Compton, Electrocatalysis at graphite and carbon nanotube modified electrodes: edge-plane sites and tube ends are the reactive sites, Chem. Commun. (2005) 829–841, https://doi.org/10.1039/B413177K.

[20] E. Leppänen, M. Akhoundian, S. Sainio, J. Etula, O. Pitkänen, T. Laurila, Structure-property relationships in carbon electrochemistry, Carbon N. Y. 200 (2022) 375–389, https://doi.org/10.1016/j.carbon.2022.08.076.

[21] E. Leppänen, S. Sainio, H. Jiang, B. Mikladal, I. Varjos, T. Laurila, Effect of electrochemical oxidation on physicochemical properties of Fe-containing single-walled carbon nanotubes, ChemElectroChem. 7 (2020) 4136–4143, https://doi.org/10.1002/celc.202000878.

[22] E. Leppänen, J. Etula, P. Engelhardt, S. Sainio, H. Jiang, B. Mikladal, A. Peltonen, I. Varjos, T. Laurila, Rapid industrial scale synthesis of robust carbon nanotube network electrodes for electroanalysis, J. Electroanal. Chem. 896 (2021), 115255, https://doi.org/10.1016/j.jelechem.2021.115255.

[23] S. Sainio, N. Wester, A. Aarva, C.J. Titus, D. Nordlund, E.I. Kauppinen, E. Leppänen, T. Palomäki, J.E. Koehne, O. Pitkänen, K. Kordas, M. Kim, H. Lipsanen, M. Mozetič, M.A. Caro, M. Meyyappan, J. Koskinen, T. Laurila, Trends in carbon, oxygen, and nitrogen core in the X-ray absorption spectroscopy of carbon nanomaterials: a guide for the perplexed, J. Phys. Chem. C 125 (2021) 973–988, https://doi.org/10.1021/acs.jpcc.0c08597.

[24] A. Moisala, A.G. Nasibulin, D.P. Brown, H. Jiang, L. Khriachtchev, E.I. Kauppinen, Single-walled carbon nanotube synthesis using ferrocene and iron pentacarbonyl in a laminar flow reactor, Chem. Eng. Sci. 61 (2006) 4393–4402, https://doi.org/10.1016/j.ces.2006.02.020.

[25] P. Engelhardt, Electron tomography of chromosome structure, Encycl. Anal. Chem. (2006), https://doi.org/10.1002/9780470027318.a1405.

[26] P. Engelhardt, Three-dimensional reconstruction of chromosomes using electron tomography, in: J. Kuo (Ed.), Electron Microscopy: Methods and Protocols, Humana Press, Totowa, NJ, 2007, pp. 365–385, https://doi.org/10.1007/978-1-59745-294-6_18.

[27] T.J. Regan, H. Ohldag, C. Stamm, F. Nolting, J. Lüning, J. Stöhr, R.L. White, Chemical effects at metal/oxide interfaces studied by X-ray-absorption spectroscopy, Phys. Rev. B. 64 (2001), 214422, https://doi.org/10.1103/PhysRevB.64.214422.

[28] M.S. Dresselhaus, G. Dresselhaus, R. Saito, A. Jorio, Raman spectroscopy of carbon nanotubes, Phys. Rep. 409 (2005) 47–99, https://doi.org/10.1016/j.physrep.2004.10.006.

[29] D.H. Kim, H.J. Lee, G. Kim, Y.S. Koo, J.H. Jung, H.J. Shin, J.-Y. Kim, J.-S. Kang, Interface electronic structures of $BaTiO_3$@X nanoparticles (X=γ-Fe_2O_3, Fe_3O_4, α-Fe_2O_3, and Fe) investigated by XAS and XMCD, Phys. Rev. B. 79 (2009) 33402, https://doi.org/10.1103/PhysRevB.79.033402.

[30] K. Kuepper, I. Balasz, H. Hesse, A. Winiarski, K.C. Prince, M. Matteucci, D. Wett, R. Szargan, E. Burzo, M. Neumann, Electronic and magnetic properties of highly ordered Sr2FeMoO6, Phys. Status Solidi 201 (2004) 3252–3256, https://doi.org/10.1002/pssa.200405432.

[31] J.P. Crocombette, M. Pollak, F. Jollet, N. Thromat, M. Gautier-Soyer, X-ray-absorption spectroscopy at the Fe L2,3 threshold in iron oxides, Phys. Rev. B. 52 (1995) 3143.

[32] A. Furlan, U. Jansson, J. Lu, L. Hultman, M. Magnuson, Structure and bonding in amorphous iron carbide thin films, J. Phys. Condens. Matter 27 (2015), 045002, https://doi.org/10.1088/0953-8984/27/4/045002.

[33] H. Ikeno, I. Tanaka, T. Miyamae, T. Mishima, H. Adachi, K. Ogasawara, First principles calculation of Fe $L_{2,3}$-edge X-ray absorption near edge structures of iron oxides, Mater. Trans. 45 (2004) 1414–1418, https://doi.org/10.2320/matertrans.45.1414.

[34] P.S. Miedema, F.M.F. de Groot, The iron L edges: Fe 2p X-ray absorption and electron energy loss spectroscopy, J. Electron. Spectros. Relat. Phenomena 187 (2013) 32–48, https://doi.org/10.1016/j.elspec.2013.03.005.

[35] J.-Y. Kim, T.Y. Koo, J.-H. Park, Orbital and bonding anisotropy in a half-filled $GaFeO_3$ magnetoelectric ferrimagnet, Phys. Rev. Lett. 96 (2006) 47205, https://doi.org/10.1103/PhysRevLett.96.047205.

[36] C.T. Wirth, B.C. Bayer, A.D. Gamalski, S. Esconjauregui, R.S. Weatherup, C. Ducati, C. Baehtz, J. Robertson, S. Hofmann, The phase of iron catalyst nanoparticles during carbon nanotube growth, Chem. Mater. 24 (2012) 4633–4640, https://doi.org/10.1021/cm301402g.

[37] L.F. Pascual, I. Pande, A. Kousar, S. Rantataro, T. Laurila, Nanoscale engineering to control mass transfer on carbon-based electrodes, Electrochem. Commun. 140 (2022), 107328, https://doi.org/10.1016/j.elecom.2022.107328.

[38] A.M. Kuznetsov, J. Ulstrup, Electron Transfer in Chemistry and Biology: An Introduction to the Theory, John Wiley & Sons Ltd, 1999.

[39] R.S. Nicholson, Theory and application of cyclic voltammetry for measurement of electrode reaction kinetics, Anal. Chem. 37 (1965) 1351–1355, https://doi.org/10.1021/ac60230a016.

[40] H. Matsuda, Y. Ayabe, Theoretical analysis of polarographic waves. I. Reduction of simple metal ions, Bull. Chem. Soc. Jpn. 28 (1955) 422–428, https://doi.org/10.1246/bcsj.28.422.

[41] Y. Wang, J.G. Limon-Petersen, R.G. Compton, Measurement of the diffusion coefficients of [Ru(NH3)6]3+ and [Ru(NH3)6]2+ in aqueous solution using microelectrode double potential step chronoamperometry, J. Electroanal. Chem. 652 (2011) 13–17, https://doi.org/10.1016/j.jelechem.2010.12.011.

[42] S.J.C. Weusten, M.T. de Groot, J. van der Schaaf, A comparative study of the stability of hexachloroiridate and hexacyanoferrate in electrochemical mass transfer measurements, J. Electroanal. Chem. 878 (2020), 114512, https://doi.org/10.1016/j.jelechem.2020.114512.

[43] S. Trasatti, E. Lust, The potential of zero charge, in: R.E. White, J.O. Bockris, B. E. Conway (Eds.), Modern Aspects of Electrochemistry vol. 33, Springer US, Boston, MA, 2002, pp. 1–215, https://doi.org/10.1007/0-306-46917-0_1.

[44] O.A. Petrii, Surface electrochemistry of oxides: thermodynamic and model approaches, Electrochim. Acta. 41 (1996) 2307–2312, https://doi.org/10.1016/0013-4686(96)00060-6.

[45] P. Gilli, L. Pretto, V. Bertolasi, G. Gilli, Predicting hydrogen-bond strengths from acid−base molecular properties. The pKa slide rule: toward the solution of a long-lasting problem, Acc. Chem. Res. 42 (2009) 33–44, https://doi.org/10.1021/ar800001k.

[46] T. Palomäki, S. Chumillas, S. Sainio, V. Protopopova, M. Kauppila, J. Koskinen, V. Climent, J.M. Feliu, T. Laurila, Electrochemical reactions of catechol, methylcatechol and dopamine at tetrahedral amorphous carbon (ta-C) thin film electrodes, Diam. Relat. Mater. 59 (2015) 30–39, https://doi.org/10.1016/j.diamond.2015.09.003.